Optik 158 (2018) 199–203

Contents lists available at ScienceDirect

Optik

journal homepage: www.elsevier.de/ijleo

Original research article

Effect of the synthesis conditions on the structural, morphological and optical properties of $Bi_2Te_{2.7}Se_{0.3}$ nanoparticles

H.M. Ali, E.M.M. Ibrahim*, M.M. Wakkad, M.A.A. Mohamed

Physics Department, Faculty of Science, Sohag University, Sohag 82524, Egypt

ARTICLE INFO

Article history:
Received 12 November 2017
Accepted 19 December 2017

Keywords:
Bi_2Te_3
Physical vapour deposition
Optical
Chalcogenide
Kubelka-Munk theory

ABSTRACT

Beside their promising utility as thermoelectric generators, Bi_2Te_3 and related compounds have several applications in electronic and optoelectronic devices. In this work, $Bi_2Te_{2.7}Se_{0.3}$ nanoparticles (NPs) were successfully prepared via physical vapor deposition technique at different conditions of flow rate and temperature. The x-ray diffraction patterns show that, the NPs crystallize in a rhombohedral crystal structure with preferable growth along the (015) plane. Field-emission scanning electron microscope (FE-SEM) investigation shows that the NPs size depends significantly on the synthesis conditions of flow rate and temperature where it decreases with the decrease in the former or with the increase in the later. The effect of deposition conditions on the final morphology can be interpreted through the accompanied variation in the concentration of the gaseous precursors in the hot zone. The optical properties were studied using Kubelka-Munk theory. Optical band gaps of 0.52, 0.58, 0.53 eV were determined for the samples synthesized under different conditions.

1. Introduction

Bi_2Te_3 and its based solid solutions are layered structure with rhombohedral unit cell (space group:R-3m) such that the bismuth and tellurium atoms are arranged in parallel layers following the sequence $Te^{(1)}$-Bi-$Te^{(2)}$–Bi-Te [1] which is continually repeated [1]. In addition to their efficiency as thermoelectric materials [2–5] which culminated in the fabrication of thermoelectric generator and thermo-coolers, these compounds have several applications in electronics, microelectronics, optoelectronics and electromechanical devices [6]. For example, such compounds are used as photoconductive targets in TV cameras, IR spectroscopy, IR detectors and sensors [7–10]. Also, Bi_2Te_3 is a narrow band gap semiconductor and thus it could be exploited in other applications like temperature controller in laser diode [11] and optical recording system [12]. According to the presence of point defects, Bi_2Te_3 can exhibit either p- or n- type conduction but n-type is the most common as a result of considerable amount of anti-site point defects through the occupying of Te site with bismuth site [6].There are several strategies that were introduced to improve the thermoelectric performance of Bi_2Te_3 like doping, nanostructuring and nanocomposites [13].

Indeed, a great enhancement was achieved especially in nanostructures which can be attributed to the increase of density of states (DOS) and the decrease in the thermal conductivity through the scattering of the phonons across the boundaries [14]. Doping with antimony (Sb) [15] and selenium (Se) [16] is adopted strategy in order to enhance the physical properties of

* Corresponding author.
E-mail address: e.ibrahim@science.sohag.edu.eg (E.M.M. Ibrahim).

https://doi.org/10.1016/j.ijleo.2017.12.090
0030-4026/

Bi_2Te_3. There are various techniques that are used for the synthesis of Bi_2Te_3 based compounds such as thermal evaporation [17], co-sputtering [18] molecular beam epitaxy [19], solvothermal method [20],etc. In this work, $Bi_2Te_{2.7}Se_{0.3}$ compound has been synthesized by physical vapor deposition (PVD) method. Although, this compound has fuelled an intense research as an efficient thermoelectric material, few papers that focused on studying the effect of deposition on its structure, morphology and optical properties which have been presented here.

2. Experimental method

$Bi_2Te_{2.7}Se_{0.3}$ NPs were synthesized from a bulk alloy as a source material using the physical vapor deposition (PVD) technique and the procedures can be summarized as the following: (i) The source material was placed in the hot zone at a certain temperature (T) to transform the solidus material to gaseous phase. (ii) Argon gas (Ar) was used as a carrier gas to transport the NPs formed in the gaseous phase to the cold zone. (iii) The $Bi_2Te_{2.7}Se_{0.3}$ NPs were deposited on glass substrates placed in the cold zone at temperature not higher than 200 °C. (iv) After furnace cooling to the room temperature, the deposited NPs were extracted from the cold zone for carrying out the various investigations and measurements.

Noteworthy, three samples of deposited $Bi_2Te_{2.7}Se_{0.3}$ NPs were synthesized at different conditions of temperature and flow rate, specifically, (1035 °C, 270 SCCM), (825 °C, 270 SCCM) and (825 °C, 225 SCCM) and denoted in the following as sample A–C, respectively as a matter of facilitation. The samples were characterized using the x-ray diffraction (XRD) (Brucker Axs-D8 Advance diffractometer with Cu-K_α radiation at $\lambda = 0.154178$ nm). The surface morphology and structure were demonstrated using scanning electron microscope (SEM) model: Quanta FEG250 for imaging the surface morphology. To study the optical properties of the synthesized samples, A Jascov-570 UV–vis-NIR spectrophotometer was employed to record the reflection spectrum over the wavelength range 200–2500 nm at both normal incidence and room temperature. Diffuse reflectance spectrum was obtained using a diffuse reflectance accessory model ISN-470, and the reflectance was converted by the instrument software to F(R) values according to Kubelka-Munk method.

3. Results and discussion

3.1. Structure and morphology

3.1.1. Effect of deposition conditions on the structure

Fig. 2a shows the XRD pattern of the synthesized samples A–C. The data confirm that the NPs for all samples crystallize in polycrystalline rhombohedral structure with preferential orientation along (015) direction. With respect to the sample (A), all peaks can be indexed to Bi_2Te_3 compound with preferable growth through (015) plane. The peaks can be indexed using standard reflection data of JCPDS card no. 85–0439. The sharpness of the peaks confirms the good crystallinity of the products. No additional peaks correspond to Te, Se, Bi or other impurities were observed indicating to the high purity of the sample.

The x-ray pattern of sample (B) reveals that the phase is Te-rich Bi_2Te_3 indicating the simultaneous co-existence of Bi_2Te_3 and Te atoms (denoted by *). Additional small peak corresponding to Bi (denoted by ♦) could be observed. Noteworthy, the strong appearance of Te peaks here can be attributed to the decrease in temperature in the hot zone. Where, once the thermal decomposition of the bulk alloy occurs, the elements begin to evaporate with different evaporation rate [21]. The decrease in temperature with fixing the flow rate of argon leads to a reduce in the concentration of the gaseous precursors in the hot zone and hence, the chance of Bi atom to meat and react with Te atom in the hot zone decreases which make limitation for the growth of Bi_2Te_3 phase. This hypothesis is also assured if we take in consideration that the nucleation and growth of Te atoms is faster than Bi_2Te_3 [22].

The x-ray data of sample (C) illustrates a decrease in the intensity of the Bi and Te peaks as shown in Fig. 2a. The reason for the lack of Te and Bi phases here can be attributed to the increase of the concentration of gaseous precursors in the hot zone compared to sample (B) due to the decrease in the flow rate which leads to the increase of the chance of Bi and Te atoms to react and form Bi_2Te_3 compound.

The average crystallite size (D_{XRD}) was calculated using Debye–Sherrer's equation [23] $D = 0.9\lambda/\beta \cos\theta$ where, θ is the glancing angle, λ is the wavelength of Cu k_α radiation ($\lambda = 1.5406$ Å) and β is the full width at half maximum. Also, The dislocation density(ρ) which assess the proportion of defects through the samples is calculated using this formula $\rho = 1/(D_{XRD})^2$ [24]. It is well known that as the crystallite size becomes smaller the lattice strain (ε) becomes larger and the x-ray diffraction peak becomes broader [25]. The strain is calculated using this formula $\varepsilon = \beta \cos\theta/4$ [26]. All the previously mentioned x-ray parameters are tabulated in Table 1.

Table 1
XRD parameters of the synthesized samples.

Sample	FWHM	D_{XRD}(nm)	ρ $(nm)^{-2}$ $(10)^{-3}$	ε $(10)^{-3}$
(A)	0.478	17.22	3.3	2
(B)	0.299	27.48	1.3	1.2
(C)	0.276	29.77	1.1	1.1

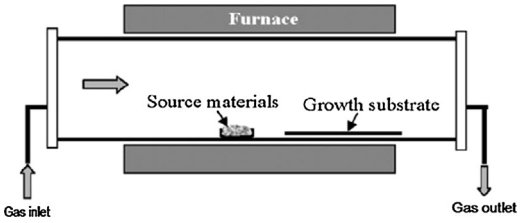

Fig. 1. shows a schematic diagram of PVD system.

According to the XRD parameters, one can observe that with decreasing temperature or flow rate the D_{XRD} increases and this can be attributed to the resultant decrease of the density of species in the hot zone. Also, the ρ decreases with the decrease in either temperature or flow rate as a result to the crystallization process becomes more slower. In addition, as it is expected [25], a decrease in the lattice strain was found with the decrease in either temperature or flow rate due to the decrease in the dislocation density.

3.1.2. Effect of deposition conditions on the morphology

Field emission scanning electron microscope (FE-SEM) images as shown in Fig. 1(a–c) show that the synthesis conditions of temperature and flow rate have a significant effect on the final morphology of the products. To be specific, the images illustrate that the $Bi_2Te_{2.7}Se_{0.3}$ consist of spherical NPs, but both of the average size and size distribution depend on the synthesis temperature and flow rate. The histograms depicted as insets in Fig. 1(a–c) reveal that the particles of sample (A) have much larger average size (~600 nm) compared to that of sample (B) (~228 nm). This can be attributed to the high synthesis temperature (1035 °C) which led to a high evaporation rate of the source material and thus a high concentration of the gaseous precursors in the reactor during the synthesis process. Also, due to high temperature in the reactor, the tiny particles coalesce in large particles due to the repining effect and growth continuation. In contrast, as the temperature was fixed at 825 °C (samples (B) and (C)), the decrease in the flow rate from 270 to 225 SCCM results in an increase in the particle size from ~228 to 379 nm. This can be interpreted as the following: by decreasing the flow rate, the time of survival of the

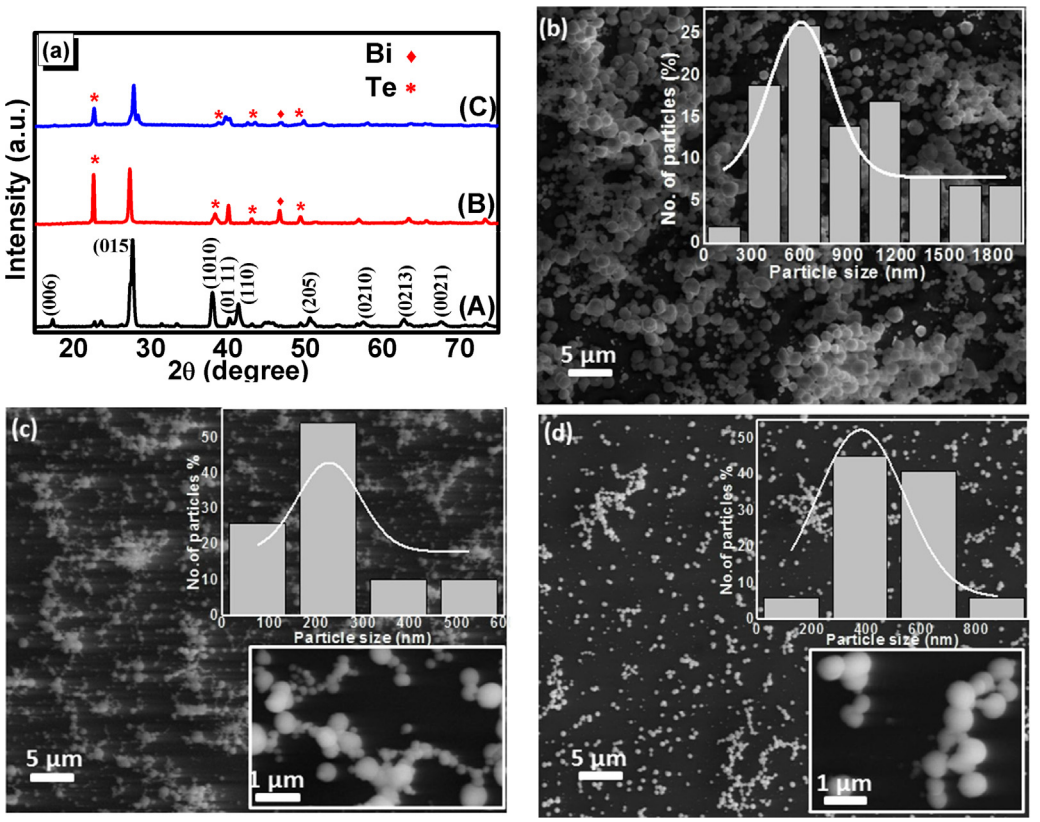

Fig. 2. XRD patterns (a), FE-SEM (b–d) corresponding to the samples A–C, respectively, of $Bi_2Te_{2.7}Se_{0.3}$ NPs. Insets in Figs. b–d show the particle size distribution of the prepared samples.

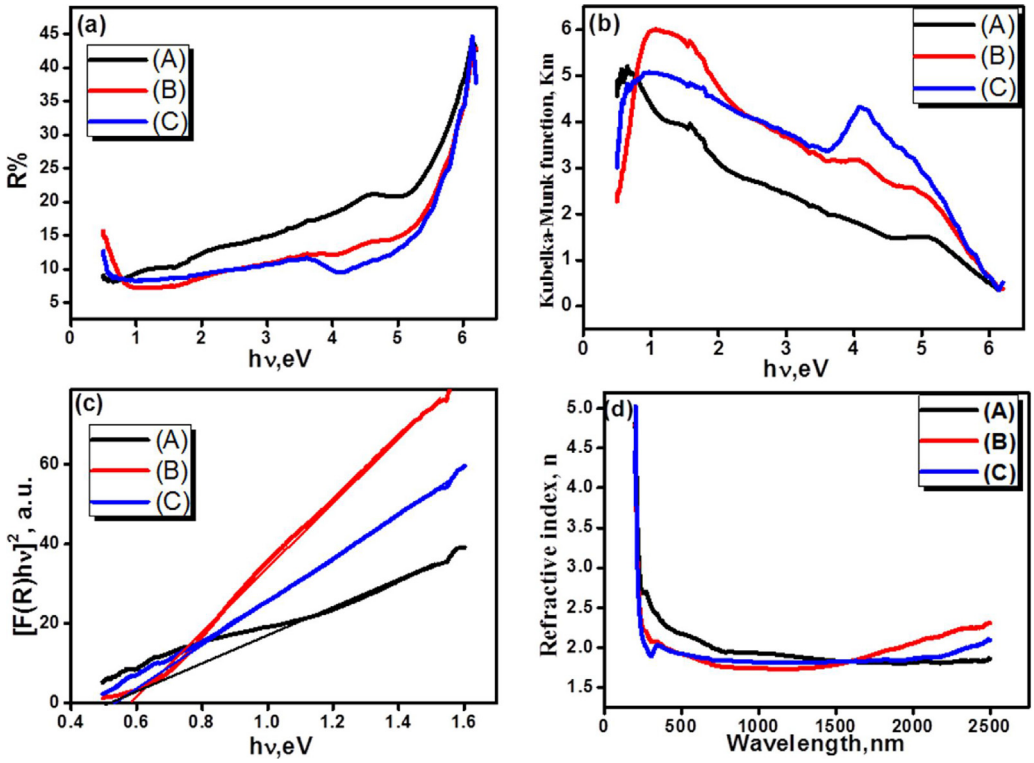

Fig. 3. the variation of diffuse reflection spectrum (a), Kubelka-Munk function (b), $[F(R)h\nu]^2$ versus $h\nu$ (c), wavelength dependence of the refractive index (d).

gaseous precursor in the hot zone becomes larger and tiny particles will coalesce to each other leading to the formation of larger particle size [27–28]

3.2. Optical properties

Diffuse reflection spectrum of the samples under study were recorded at room temperature as shown in Fig. 3a, then converted to absorption spectrum, as shown in Fig. 3b, by employing Kubelka–Munk theory [29–30] using the formula: $F(R) = \alpha = (1\text{-}R)^2/2R$, where α is the absorption coefficient, R is the diffuse reflection factor and F(R) is the Kubelka-Munk function. Using the calculated optical absorption coefficient through Kubelka–Munk theory, the optical band gap of $Bi_2Te_{2.7}Se_{0.3}$ specimens were determined using Tauc's law [31–32] $[F(R)h\nu]^n = \beta(h\nu\text{-}E_{op})$ in which $h\nu$, β, and E_{op} are the incident photon energy, proportionality constant, and optical band gap, respectively. The exponent n equals 2 or 1/2 for direct or indirect transitions, respectively. By extrapolating the linear portion of the plots of $[F(R)h\nu]^2$ and $[F(R)h\nu]^{1/2}$ versus $h\nu$ (see Fig. 3c), the optical band gap (E_{op}) could be determined as shown in Fig. 2c.The calculated optical band gaps are 0.52, 0.58, 0.53 eV for samples (A)–(C), respectively.

These values are larger than the values calculated for the bulk Bi_2Te_3 (0.15 eV) and this can be ascribed to both of the incorporation of Se instead of Te [33] in its lattice and the quantum confinement effects resulting from the nano-sized dimensions [34]. Kadhim et al. reported an optical band gap of 0.43 eV for Bi_2Te_3 which increased to 0.73 eV with Se incorporation [33]. Also, Zimmer et al. [35] determined a direct optical band gap of 0.6 eV for $Bi_2Te_{2.7}Se_{0.3}$ thin film. It is worth mentioning that, in this work, the maximum value of the optical band gap (0.58 eV) was obtained for sample (B) and this can be attributed to both of the smaller particle size than samples A and C and the extra existence of unreacted Te atoms in it. The refractive index (*n*) of $Bi_2Te_{2.7}Se_{0.3}$ samples at hand were calculated as presented elsewhere [36], and the corresponding average values of refractive index are 2.12, 1.88 and 1.9 in the visible regions and 1.82, 2 and 1.87 near infrared for samples (A)–(C), respectively (see Fig. 3d). The free carrier concentration (N) was estimated optically according to Drud's model as presented elsewhere [37]. The corresponding value of N for $Bi_2Te_{2.7}Se_{0.3}$ samples were found to be equal to 3.59×10^{19}, 1.75×10^{20} and 3.14×10^{19} cm^{-3} for the samples A–C, respectively.

4. Conclusion

$Bi_2Te_{2.7}Se_{0.3}$ nanoparticles (NPs) were successfully prepared using physical vapor deposition (PVD) technique at different conditions of temperature and flow rate. XRD patterns confirm that the structure of the NPs is polycrystalline in nature and

having rhombohedral crystal structure. The effect of deposition conditions on the internal structure and morphology was studied in detail. It was found that a significant decrease in the particle size can be obtained with a decrease in the temperature or an increase in the flow rate. Optical band gaps of 0.52, 0.58, 0.53 eV for the samples were calculated using Kubelka-Munk model. The difference in the value of the optical band gaps can be ascribed to the difference in both of the particle size and the proportion of unreacted Te atoms within the material. So, to obtain $Bi_2Te_{2.7}Se_{0.3}$ NPs with desired purity, structure and morphology, the deposition conditions should be optimized. Our samples can be employed in several applications in optoelectronic devices.

References

[1] D.M. Rowe, CRC Handbook of Thermoelectrics, Macro to Nano, CRC Press, Taylor & Francis Group, 2006.
[2] D.A. Wright, Nature 181 (1958) 834.
[3] L. Britnell, R. Ribeiro, A. Eckmann, R. Jalil, B. Belle, A. Mishchenko, Y.J. Kim, R. Gorbachev, T. Georgiou, S. Morozov, Science 340 (2013) 1311–1314.
[4] E.M.M. Ibrahim, A.M.A. Hakeem, A.M.M. Adam, E.S. Shokr, Phys. Scr. 90 (4) (2015) 45802.
[5] M.M. Ibrahim, E.M.M. Ibrahim, S.A. Saleh, A.M.A. Hakeem, J. Alloys Compd. 429 (1) (2007) 19–24.
[6] B. Jariwala, D. Shah, N.M. Ravindra, Thin Solid Films 589 (2015) 396–402.
[7] D. Arivuoli, F.D. Gnanam, P. Ramasamy, J. Mater. Sci. Lett. 7 (1988) 711–713.
[8] N. Sakai, T. Kajiwara, K. Takemura, S. Minomura, Y. Fujii, Solid State Commun. 40 (1981) 1045–1047.
[9] M. Stölzer, M. Stordeur, H. Sobotta, V. Riede, Phys. Status Solidi B 138 (1986) 259.
[10] L. Jansa, P. Lošťák, J. Šrámková, J. Horák, J. Mater. Sci. 27 (1992) 6062–6066.
[11] D.M. Rowe, C.M. Bhandari, Modern Thermoelectrics, Reston Publishing Company, Reston, VA, 1983.
[12] K. Watanabe, N. Sato, S. Miyaoka, J. Appl. Phys. 54 (1983) 1256.
[13] C. Gayner, K.K. Kar, Prog. Mater. Sci. 83 (2016) 330–382.
[14] B. Poudel, Q. Hao, Y. Ma, Y. Lan, A. Minnich, B. Yu, X. Yan, D. Wang, A. Muto, D. Vashaee, X. Chen, J. Liu, M.S. Dresselhaus, G. Chen, Z. Ren, Science 320 (2008) 634–638.
[15] B. Bochentyn, T. Miruszewski, J. Karczewski, B. Kusz, Mater. Chem. Phys. 177 (2016) 353–359.
[16] S. Wang, W. Xie, H. Li, X. Tang, Intermetallics 19 (2011) 1024–1031.
[17] H.E.A. El-Sayed, Appl. Surf. Sci. 250 (2005) 70.
[18] D.-H. Kim, E. Byon, G.-H. Lee, S. Cho, Thin Solid Films 510 (2006) 148.
[19] H.W. Liu, H.T. Yuan, N. Fukui, L. Zhang, J.F. Jia, Y. Iwasa, M.W. Chen, T. Hashizume, T. Sakurai, Q.K. Xue, Cryst. Growth Des. 10 (2010) 4491.
[20] J. Guo, J. Jian, Z. Zhang, R. Wu, J. Li, Y. Sun, J. Cryst. Growth 434 (2016) 1–6.
[21] S.A. Ahmed, E.M.M. Ibrahim, S.A. Saleh, Appl. Phys. A 85 (2006) 177.
[22] Y. Xu, Z. Ren, W. Ren, K. Deng, Y. Zhong, Mater. Lett. 62 (2008) 763.
[23] P. Debye, Z. von röntgenstrahlen, Ann. Phys. 351 (1915) 809–823.
[24] Y. Badr, I.K. Battisha, A.M.S. El Nahrawy, B. Elouadi, M. Kamal, N.J. Glas, Ceramics 1 (2011) 71.
[25] F. Gu, S.F. Wang, M.K. Lu, G.J. Zhou, D. Xu, D.R. Yuan, J. Phys. Chem.B 108 (2004) 8119.
[26] H.M. Ali, S.A. Saleh, Thin Solid Films 556 (2014) 552–559.
[27] Vyacheslav O. Khavrus, E.M.M. Ibrahim, Albrecht Leonhardt, Silke Hampel, Steffen Oswald, Christine Täschner, Bernd Büchner, J. Phys. Chem. C 114 (2009) 843–848.
[28] T. Jaumann, E.M.M. Ibrahim, S. Hampel, D. Maier, A. Leonhardt, B. Büchner, Chem. Vap. Deposition 19 (7–9) (2013) 228–234.
[29] H.M. Ali, M.M. Abou-Mesalam, M.M. El-Shorbagy, J. Phys. Chem. Solids 71 (2010) 51.
[30] C. Karunakaran, S.S. Raadha, P. Gomathisankar, J. Alloy. Compd. 549 (2013) 269.
[31] J. Tauc, Amorphous and Liquid Semiconductors, Plenum Press, London and New York, 1974.
[32] G. Saffarini, J.M. Saiter, H. Schmitt, Opt. Mater. 29 (2007) 1143.
[33] A. Kadhim, A. Hmood, H. Abu Hassan, Mater. Lett. 65 (2011) 3105–3108.
[34] P. Srivastava, K. Singh, J. Exp. Nanosci. 9 (2014) 1064–1074.
[35] A. Zimmer, N. Stein, H. Terryn, C. Boulanger, J. Phys. Chem. Solids 68 (2007) 1902–1907.
[36] H.M. Ali, M.M. Abou-Mesalam, M.M. El-Shorbagy, J. Phys. Chem. Solids 71 (2010) 51.
[37] C. Nahm, S. Shin, W. Lee, J.I. Kim, D.-R. Jung, J. Kim, S. Nam, S. Byun, B. Park, Curr. Appl. Phys. 13 (2013) 415–418.